Nanostructuring mixed-dimensional perovskites : a route toward tunable, efficient photovoltaics

Koh, Teck Ming; Shanmugam, Vignesh; Schlipf, Johannes; Oesinghaus, Lukas; Müller-Buschbaum, Peter; Ramakrishnan, N.; Swamy, Varghese; Mathews, Nripan; Boix, Pablo P.; Mhaisalkar, Subodh Gautam

2016

Koh, T. M., Shanmugam, V., Schlipf, J., Oesinghaus, L., Müller-Buschbaum, P., Ramakrishnan, N., . . . Mhaisalkar, S. G. (2016). Nanostructuring mixed-dimensional perovskites : a route toward tunable, efficient photovoltaics. Advanced Materials, 28(19), 3653-3661. doi:10.1002/adma.201506141

https://hdl.handle.net/10356/142102

https://doi.org/10.1002/adma.201506141

Nanostructuring Mixed-Dimensional Perovskites: A Route Toward Tunable, Efficient Photovoltaics

Teck Ming Koh, Vignesh Shanmugam, Johannes Schlipf, Lukas Oesinghaus, Peter Müller-Buschbaum, N. Ramakrishnan, Varghese Swamy, Nripan Mathews, Pablo P. Boix,* and Subodh G. Mhaisalkar*

2D perovskites is one of the proposed strategies to enhance the moisture resistance, since the larger organic cations can act as a natural barrier. Nevertheless, 2D perovskites hinder the charge transport in certain directions, reducing the solar cell power conversion efficiency. A nanostructured mixed-dimensionality approach is presented to overcome the charge transport limitation, obtaining power conversion efficiencies over 9%.

Hybrid organic–inorganic halide perovskites have attracted overwhelming attention over the past three years, achieving unprecedented photovoltaic performance[1-4] in solution-processed solar cells. In spite of the rapid growth in this area, primarily 3D perovskites with the general form of ABX_3 ($A = Cs^+$, $CH_3NH_3^+$, $HC(NH_2)_2^+$; $B = Pb^{2+}$, Sn^{2+}, Ge^{2+}; $X = Cl^-$, Br^-, I^-) have been studied as light harvesters in solid-state devices.[5] In particular, the 3D perovskite methylammonium lead iodide ($CH_3NH_3PbI_3$) has represented the archetypical material of interest, combining ideal light absorber characteristics (high optical absorption,[1] low trap densities,[6, 7] and remarkable diffusion lengths[6, 8, 9]) with solution processability.

Despite the promising progress in improving the efficiency of $CH_3NH_3PbI_3$ solar cells, their long-term stability is yet one of the major challenges to be addressed. Several reports have shown that the instability of perovskite film can be triggered by moisture and oxygen,[10, 11] additives in hole transporting layer,[12] light exposure,[13] or UV irradiation.[14] Some techniques employed to improve their long-term stability include Al_2O_3 postmodification on $CH_3NH_3PbI_3$,[10] TiO_2 scaffold replaced with Al_2O_3 to avoid UV-induced instability[14] and halide substitution.[15] More recently, 2D perovskite systems have been introduced as light absorbers in photovoltaics due to the higher moisture resistance attributed to them.[16, 17]

Lower dimensional perovskites are generally derived from their 3D counterparts (ABX_3) by increasing the distance between the interconnected inorganic sheets with the appropriate organic cations along the 〈100〉 direction, giving the general formula of $A_2A'_{n-1}B_nX_{3n+1}$ where A and A′ represent organic cations, B represents divalent metal ions, and X represents halide ions. **Scheme 1** shows the schematic illustration of crystalline structure of 2D, mixed-dimensionality, and 3D perovskites. The binding energy and band gap of perovskite is reduced as the dimensionality is increased. In order to achieve reasonable band gap of perovskite suitable for photovoltaic application while promoting the moisture resistance, mixed-dimensionality approach becomes one of the solutions. In 2D perovskite systems, the size constraints derived from the Goldschmidt's tolerance factor are relaxed, and larger organic cations can be incorporated into the structure. Varying the stacking of the metal halide lattices (n) in 2D perovskite could change the dimensionality and modulate the exciton binding energy as well as its bandgap,[18, 19] making these materials very suitable for light emission and light harvesting applications. However, in photovoltaics, power conversion efficiencies based on 2D perovskite systems have been disappointing. Karunadasa and co-workers developed planar solar cells containing $(C_6H_5C_2H_4NH_3)_2(CH_3NH_3)_2Pb_3I_{10}$ layered perovskite and achieved a power conversion efficiency (PCE) of 4.73%.[16] On the other hand, Kanatzidis and co-workers have also reported the fabrication of solar cells using a 2D perovskite family, $(CH_3(CH_2)_3NH_3)_2(CH_3NH_3)_{n-1}Pb_nI_{3n+1}$ (n = 1–4) with a PCE of 4.02% measured for $(CH_3(CH_2)_3NH_3)_2(CH_3NH_3)_2Pb_3I_{10}$ perovskite.[17]

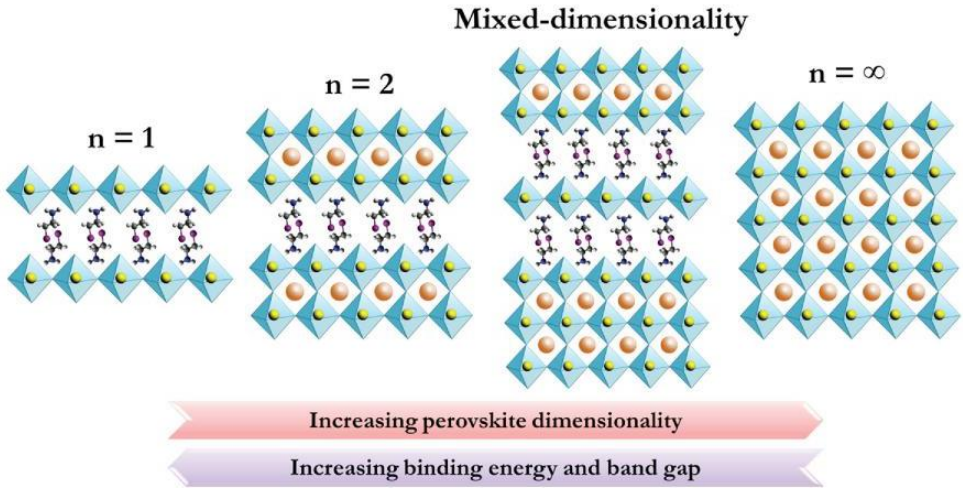

Scheme 1. Schematic illustration showing the crystalline structure of 2D perovskites (n = 1 and 2, where n represents the metal halide lattices), mixed-dimensionality perovskites and 3D perovskites ($n = \infty$).

The directionality of metal halide lattices in 2D perovskite and associated limitations in photogenerated charge transport and extraction could contribute to the low efficiencies noted till now. Generally, layered materials like 2D perovskites tend to crystallize in a direction parallel to the substrate.[20] As a consequence, the charge transport remains optimum along the metal halide lattices, whereas it gets hindered in the perpendicular directions (across the interlayers). This has been a common drawback for single-step deposited 2D perovskite solar cells,[16, 17] resulting in a relatively low fill factor (FF) and current. Thus, the use of nanostructuring to randomize the crystallizing direction of 2D perovskites represents a promising route to enhance charge transport and extraction, to deliver high device efficiency along with improved material stability.

Here, we report the controlled growth of nanostructured mixed-dimensional perovskites, $(IC_2H_4NH_3)_2(CH_3NH_3)_{n-1}Pb_nI_{3n+1}$ and its application in mesoscopic solar cells. The nanostructured perovskite films are grown using a sequential deposition method under ambient conditions in which the dimensionality of perovskite is controlled by the dipping duration. As a result, the increased n, corresponding to the enlarged stacking of the closely packed metal halide layers and a resultant smaller band gap, offers broader absorption and the possibility to achieve higher photocurrent. An overall power conversion efficiency over 9% was achieved in this novel mixed-dimensionality perovskite system, indicating the importance of nanostructuring 2D perovskites for photovoltaic applications.

Nanostructured mixed-dimensional perovskites, $(IC_2H_4NH_3)_2(CH_3NH_3)_{n-1}Pb_nI_{3n+1}$ where $n < \infty$, were obtained by sequential deposition technique. **Figure 1**a illustrates the fabrication process of the perovskite films and the resulting variety of bandgaps that are formed by the family. First, a pure 2D perovskite (n =

1) was deposited by spin coating the precursor solution containing a stoichiometric ratio of lead iodide (PbI_2) and iodoethylammonium iodide ($IC_2H_4NH_3I$) in dimethylformamide (DMF). Subsequently, the substrate was immersed into an isopropanol:toluene mixed solution containing methylammonium iodide (CH_3NH_3I) for different dipping duration (1–5 min) to increase the stacking order and convert it into higher dimensionality ($1 < n < \infty$). The mixed solvent system ensured good solubility of the CH_3NH_3I, while avoiding the redissolution of the resulting perovskite into the solvent.

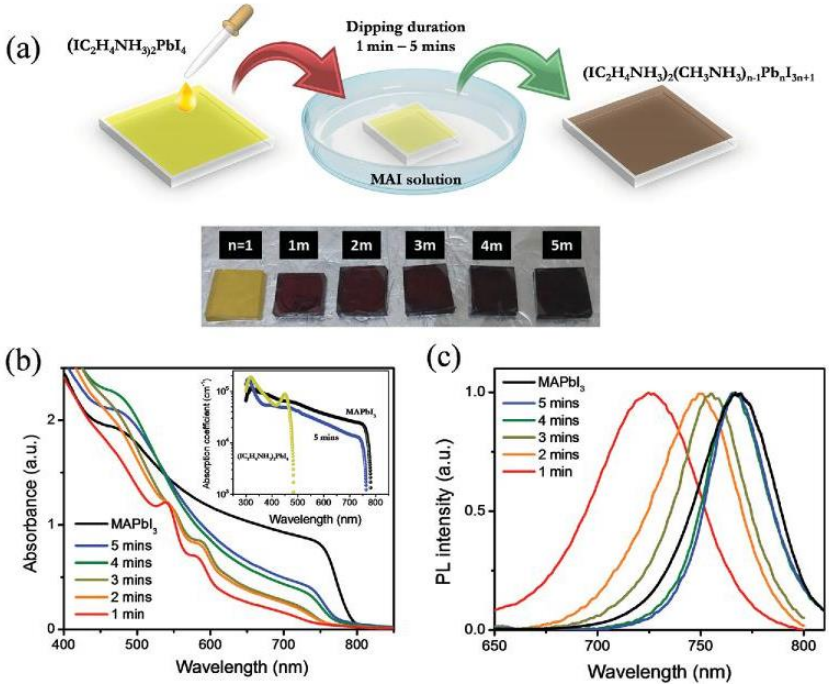

Figure 1. a) Schematic illustration of fabrication of mixed-dimensionality perovskites $(IC_2H_4NH_3)_2(CH_3NH_3)_{n-1}Pb_nI_{3n+1}$ thin films and the photographs of the perovskite films deposited in different dipping durations (1–5 min). b) Optical absorption spectra of $CH_3NH_3PbI_3$ and $(IC_2H_4NH_3)_2(CH_3NH_3)_{n-1}Pb_nI_{3n+1}$ perovskite films. Inset: absorption coefficients of $(IC_2H_4NH_3)_2PbI_4$, representative of $(IC_2H_4NH_3)_2(CH_3NH_3)_{n-1}Pb_nI_{3n+1}$ (dipping duration of 5 min) and $CH_3NH_3PbI_3$. c) PL of $(IC_2H_4NH_3)_2(CH_3NH_3)_{n-1}Pb_nI_{3n+1}$ perovskite analogues.

A suitable band gap (close to the optimum Shockley–Queisser value[21]) is desirable for high-efficiency photovoltaics. As a consequence, the fabricated pure 2D perovskite (n = 1) is not an attractive choice as light absorber due to its intrinsically larger band gap. Increasing the stacking of lead iodide lattices is one possibility to lower the band gap and simultaneously reduce the exciton binding energy for direct charge generation and separation.[5] Our approach leverages this concept, aiming at the increase of the dimensionality. Figure 1b shows the optical absorption spectra of the mixed-dimensionality $[(IC_2H_4NH_3)_2(CH_3NH_3)_{n-1}Pb_nI_{3n+1}]$ and 3D ($CH_3NH_3PbI_3$) perovskites. The characteristic absorption bands of the lower dimensionality perovskites are clearly identified for the dipping duration of 1, 2, and 3

min (ranging from 525 to 600 nm). Similar absorption behavior was previously observed in single-step prepared 2D perovskites.[16], [17], [22] As the dipping duration was increased to 4 and 5 min, these absorption bands were less noticeable, indicating the increase in the stacking of the lead halide lattices; nevertheless, there is still a clear difference in band gap between $CH_3NH_3PbI_3$ and the perovskites formed by longer dipping duration (5 min). The comparison in absorption coefficients of 3D and 2D perovskites is given in the inset of Figure 1b. Interestingly, the absorption coefficient of the fabricated 2D and mixed-dimensionality perovskite films is the same order of magnitude as the 3D $CH_3NH_3PbI_3$ perovskite, indicating that the modification of the band gap does not significantly affect the light harvesting capability. Photoluminescence (PL) spectra of the perovskite analogues of $(IC_2H_4NH_3)_2(CH_3NH_3)_{n-1}Pb_nI_{3n+1}$ are also illustrated in Figure 1c, showing the shift of PL peaks according to the band gap of each perovskite film.

In terms of crystal structures, $CH_3NH_3PbI_3$ perovskite single crystals appear as tetragonal-like structures,[23] while layered perovskites generally produce plate-like structures.[16] In 2D perovskites, the metal halide lattices favor the parallel growth to the substrate, leading to one of the main concerns of its application in PV (photovoltaic) devices: the vertical charge transport across the interlayers in the device. Therefore, controlling of the crystallization of metal halide lattices in layered perovskites becomes crucial, and nanostructuring 2D perovskites arises as a suitable option to enhance the charge transport and extraction. **Figure 2** shows the evolution of the nanostructures of $(IC_2H_4NH_3)_2(CH_3NH_3)_{n-1}Pb_nI_{3n+1}$ perovskites for two different dipping durations in the sequential technique. A complete set of field-emission scanning electron microscope (FESEM) images (from 1 to 5 min) is presented in Figures S1–S4 (Supporting Information). The immersion of the $(IC_2H_4NH_3)_2PbI_4$ into the CH_3NH_3I solution (isopropanol:toluene = 1:5) for 1 min triggers the formation of nanoplatelets on top of mesoporous TiO_2 layer. As the dipping duration increases, the nanostructures grow and the nanoplatelets are subsequently interconnected to each other, however, similar nanostructure can still be easily observed even for a dipping time of 5 min.

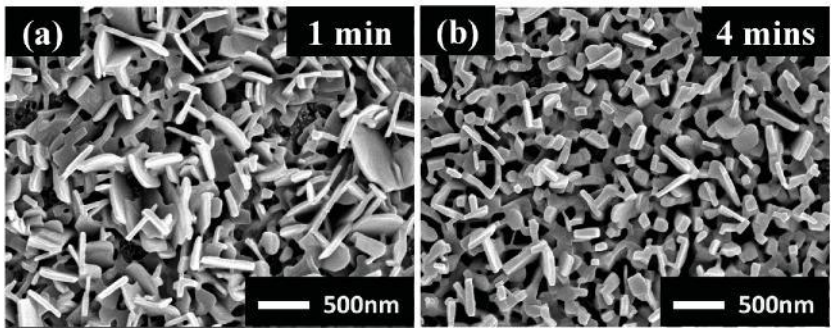

Figure 2. a,b) Top-view FESEM images of nanostructures of $(IC_2H_4NH_3)_2(CH_3NH_3)_{n-1}Pb_nI_{3n+1}$ perovskites on top of mesoporous TiO_2 layer from two different dipping durations in the sequential technique.

The X-ray diffraction (XRD) patterns of $(IC_2H_4NH_3)_2(CH_3NH_3)_{n-1}Pb_nI_{3n+1}$ perovskites on the mesoporous TiO_2 layer are displayed in **Figure 3**. The peaks around 14° and 28° are identified as the scattering from (002)/(110) and (004)/(220) crystal planes. In Figure 3b, the narrow peaks at around $2\theta \approx 14°$ indicate a

high crystallinity and coincide with the large crystal size seen in SEM images. Additionally, the intensity of the peaks increases with the sample series from 1 to 5 min dipping duration, while the position slightly moves toward smaller angles. This represents a change in crystal lattice constants, namely an expansion of the *c* -axis of the perovskite unit cell with increasing dipping duration that is responsible for the differences in band gaps.

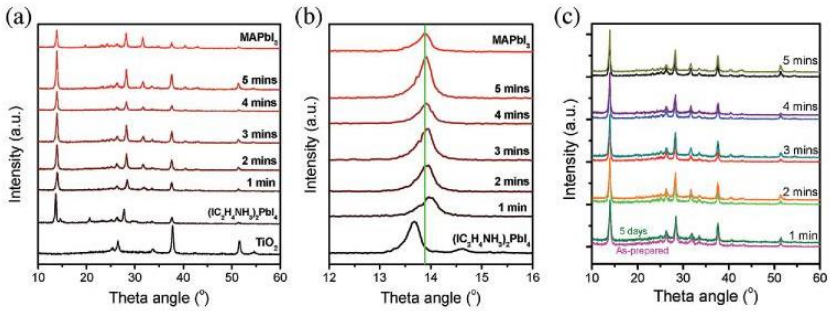

Figure 3. a,b) XRD patterns of $(IC_2H_4NH_3)_2(CH_3NH_3)_{n-1}Pb_nI_{3n+1}$ from different dipping duration, ranging from 1 to 5 min. c) Comparison of XRD patterns of as-prepared $(IC_2H_4NH_3)_2(CH_3NH_3)_{n-1}Pb_nI_{3n+1}$ perovskites films and after storing for 5 d under 40% relative humidity at 25 °C.

The instability of $CH_3NH_3PbI_3$ toward moisture is a potential barrier for the commercialization of perovskite solar cells. Mixed-dimensionality perovskites arise as a possible strategy to improve this aspect, due to the possibility of shielding the inorganic layers within judiciously chosen organic cations. In order to examine the stability, $(IC_2H_4NH_3)_2(CH_3NH_3)_{n-1}Pb_nI_{3n+1}$ perovskites were deposited on mesoporous TiO_2 layer and their XRD patterns were recorded immediately and after storing the thin films under relative humidity level of 40% at 25 °C for 5 d. The corresponding XRD patterns are illustrated in Figure **3**c. The $(IC_2H_4NH_3)_2(CH_3NH_3)_{n-1}Pb_nI_{3n+1}$ perovskites exhibit high stability and the lead iodide peak, which is the signature of $CH_3NH_3PbI_3$ decomposition, is not observed.**10**, **24**

In order to gain further insight into the crystalline information, including the orientation of the perovskite nanostructure on the substrate, grazing-incidence wide-angle X-ray scattering (GIWAXS) measurements were conducted for the mixed dimensional perovskites. The 2D GIWAXS data show Debye–Scherrer rings at the *q* values (scattering vector) expected for the tetragonal phase as seen in **Figure 4**a,b. Integration over *q* [Figure **4**c] additionally shows high background intensity for higher *q* , arising from the large surface roughness of the sample. From the higher intensity of the (002)/(110) ring around $q_r = 0$ Å^{-1} in the 2D GIWAXS data, it is apparent that 4 and 5 min samples exhibit preferential crystal orientation indicating that the crystals are oriented with the *c* -axis perpendicular toward the substrate. This is further investigated by azimuthal integration around $q = 1$ Å^{-1} [Figure **4**d] and the flanks are used to recover the inaccessible data by fitting a Gaussian peak shape. Figure **4**b clearly shows the superiority of the 4 and 5 min samples as they exhibit the strongest degree of preferential orientation. For comparison, the reported GIWAXS data of $MAPbI_3$ prepared from single-step solution-processed deposition displays a uniform distribution along

the rings and a flat intensity distribution along the azimuthal angle, indicating a completely random orientation.[25]

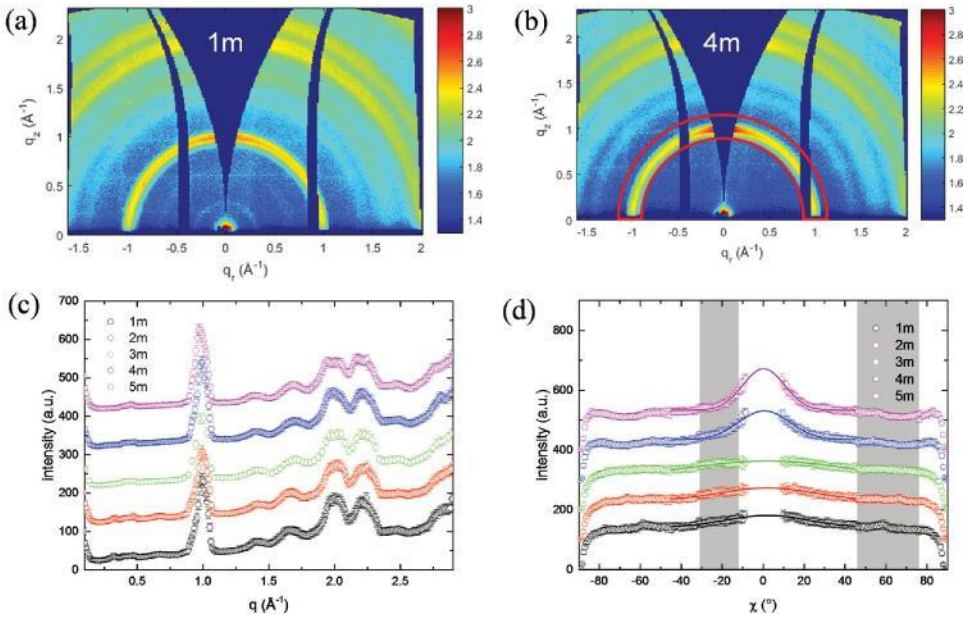

Figure 4. a,b) 2D GIWAXS data shown with logarithmic false-color scale. The inhomogeneous intensity distribution of the ring at q = 1 Å^{-1} for the 4 min sample indicates preferentially oriented crystals. The red arc indicates the azimuthal integration plotted in Figure d. c) GIWAXS data integrated over q for the sample series with increasing dipping duration. d) GIWAXS data azimuthally integrated around q = 1 Å^{-1} showing preferential orientation for the 4 and 5 min samples. Here, a Gaussian fit indicates the inaccessible data.

The energy level diagram of the components in the devices is depicted in **Figure** 5a. The HOMO (highest occupied molecular orbital) energy levels of $(IC_2H_4NH_3)_2(CH_3NH_3)_{n-1}Pb_nI_{3n+1}$ perovskites are determined from photoelectron spectroscopy in air (PESA), whereas the LUMO (lowest unoccupied molecular orbital) energy levels were estimated by subtracting band gap energy from their HOMO energy levels. The $(IC_2H_4NH_3)_2(CH_3NH_3)_{n-1}Pb_nI_{3n+1}$ perovskites were deposited on mesoporous TiO_2 layer and 2,2′,7,7′-tetrakis-(*N* ,*N* -di-4-methoxyphenylamino)-9,9′-spirobifluorene was used as hole transporter in the devices. The nanostructured $(IC_2H_4NH_3)_2(CH_3NH_3)_{n-1}Pb_nI_{3n+1}$ was fully covered by the hole transporting layer [see Figure 5b,c] as schematically illustrated in Figure 5d, however, these perovskites were not significantly affected by the employed hole transporting material (HTM) solution. Therefore, the perovskite nanoplatelets can be completely infiltrated by the hole transporting material, which facilitates the charge injection and transport and improves the device performance. This is evident from the FESEM images, where spiro-OMeTAD clearly encapsulates the perovskite layer, allowing for efficient electron and hole collection even for materials with short diffusion lengths.

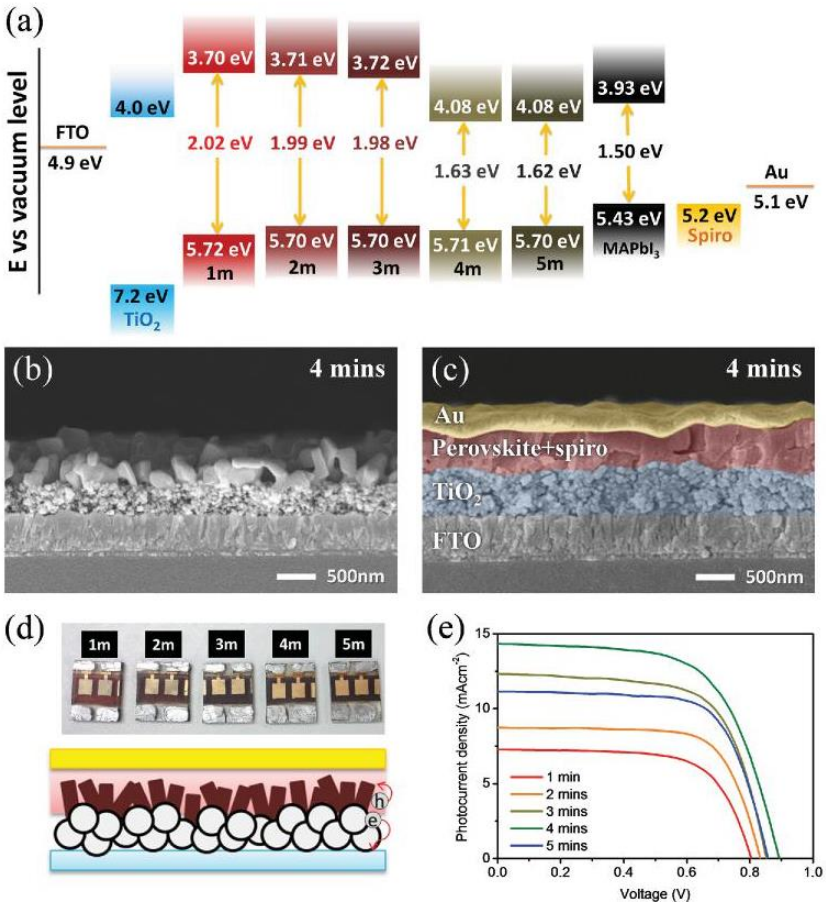

Figure 5. a) Energy diagram of solar device with $(IC_2H_4NH_3)_2(CH_3NH_3)_{n-1}Pb_nI_{3n+1}$ perovskites from different dipping duration. HOMO energy levels were determined from PESA whereas the LUMO energy levels were obtained by subtracting the bandgap from the HOMO energy level. b,c) Cross-sectional FESEM image of nanostructured $(IC_2H_4NH_3)_2(CH_3NH_3)_{n-1}Pb_nI_{3n+1}$ perovskites on top of mesoporous TiO_2 layer and complete solar device containing $(IC_2H_4NH_3)_2(CH_3NH_3)_{n-1}Pb_nI_{3n+1}$ (4 min dipping time). d) Photographs of solar cells based on $(IC_2H_4NH_3)_2(CH_3NH_3)_{n-1}Pb_nI_{3n+1}$ perovskites and the schematic diagram indicating the spiro-OMeTAD encapsulates the perovskite layer. e) Photocurrent–voltage (I–V) characteristics of the best-performing solar cells with $(IC_2H_4NH_3)_2(CH_3NH_3)_{n-1}Pb_nI_{3n+1}$ as absorbing layer, depositing from different dipping duration (light intensity: 100 mW cm^{-2}, AM1.5G). Device configuration: FTO/TiO_2 blocking layer/mesoporous TiO_2/$(IC_2H_4NH_3)_2(CH_3NH_3)_{n-1}Pb_nI_{3n+1}$/spiro-OMeTAD/Au.

As a result, the overall power conversion efficiencies of the nanostructured $(IC_2H_4NH_3)_2(CH_3NH_3)_{n-1}Pb_nI_{3n+1}$ devices improve the previous reports for 2D and mixed-dimensionality perovskite solar cells.[17, 26] The current–voltage (I–V) curves under AM1.5G illumination of the devices with $(IC_2H_4NH_3)_2(CH_3NH_3)_{n-1}Pb_nI_{3n+1}$ perovskites are plotted in Figure 5c, and the photovoltaic parameters of the best-performing solar devices from different dipping durations are summarized in **Table 1**.

Table 1. Photovoltaic parameters of the best-performing solar devices with $(IC_2H_4NH_3)_2(CH_3NH_3)_{n-1}Pb_nI_{3n+1}$ perovskites from different dipping durations. The statistics of photovoltaic parameters from a total of 31 devices are shown in Figure S4 (see the Supporting Information)

Dipping duration [min]	J_{sc} [mA cm^{-2}]	V_{oc} [mV]	FF	η [%]
1	7.28	804	0.67	3.93
2	8.76	833	0.71	5.15
3	12.32	852	0.66	6.96
4	14.33	893	0.63	8.00
5	11.51	842	0.70	6.77

In contrast, the $(IC_2H_4NH_3)_2PbI_4$ based device displays much lower performance (see Figure S5, Supporting Information), similar to the reported device performance for $(BA)_2PbI_4$ (BA is butylammonium).[17] This is expected considering the large band gap and poor charge transport through the perovskite layer. With just 1 min dipping duration, ≈4% of power conversion efficiency can be achieved. Further increasing the dipping duration produces higher photocurrent density, up to 14.33 mA cm^{-2} for the 4 min sample. Although the nanostructured morphology increasing the current is similar for all the dipping times, the small reduction of bad gap and the expected decrease of the exciton binding energy upon the increase of n justify the J_{sc} variations. Remarkably, prolonged dipping in the CH_3NH_3I solution can also cause a decrease in J_{sc}, reducing the PCE to 6.77% (5 min sample). Among all the different dipping duration, the 4 min sample exhibited the highest power conversion efficiency of 8%, significantly higher than previous 2D perovskite-based solar cells. This improvement comes mainly from the enhanced J_{sc}, which could benefit from the nanostructures of the $(IC_2H_4NH_3)_2(CH_3NH_3)_{n-1}Pb_nI_{3n+1}$ and crystal orientation observed in GIWAXS that improved the charge transport and extraction in vertical direction in the devices. In parallel, the hysteresis of the current–voltage curves is qualitatively reduced with the increasing dipping time (see Figure S6, Supporting Information), which can be tentatively related to the different crystal orientation of the formed perovskites. Further studies on this topic are currently ongoing.

The photovoltage of the devices mimics the trend of J_{sc}, increasing from 804 to 893 mV. These values represent a lower voltage compared to the conventional $CH_3NH_3PbI_3$ 3D devices. To gain more insight into the photovoltage deficit, recombination and energetic distribution of the cell were checked by impedance spectroscopy for samples with 1, 3, and 4 min dipping time. The measurements were carried out under one sun illumination, at DC voltages between short circuit and open circuit condition. The obtained Nyquist plots (see examples in the Supporting Information) were clearly dominated by the low-frequency feature, whose resistance is attributed to the recombination. Therefore, the capacitance and resistance parameters were extracted from the fitting to a simplified equivalent circuit[27] displayed in Figure S7 (Supporting Information). Interestingly, the recombination resistance (**Figure 6**a) does not show any significant

variation when the dipping time is increased. This is in good agreement with the similar morphology observed for all the analyzed samples. At the same time, the capacitance (Figure 6b) is almost one order of magnitude lower than in standard 3D perovskites (see Figure S8, Supporting Information, for reference). A similar behavior of the capacitance has been previously attributed to a contact of the HTM with the mesoporous TiO_2,[28] which also justifies the low open-circuit potential of the samples and the similar recombination resistance. These results suggest a main recombination path (TiO_2–HTM contact) similar for all the analyzed samples, such that the V_{oc} directly scales with the J_{sc}. Additional surface passivation on the TiO_2 surface may be useful to improve the photovoltage of these devices.

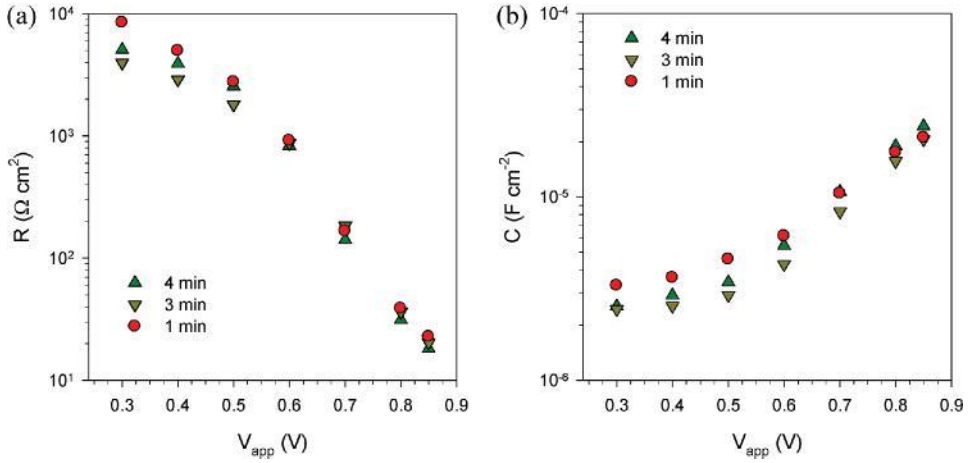

Figure 6. a) Recombination resistance and b) capacitance extracted from the fitting of the Nyquist plots with the equivalent simplified circuit in Figure S7 (Supporting Information).

The long-term stability is a common concern due to the moisture-sensitive nature of organolead halide perovskites, and the reduction of the dimensionality is a proposed approach to improve this issue. Preliminary device stability data is displayed in Figure S9 (Supporting Information). The photovoltaic parameters of the devices with perovskite films formed from different dipping durations were measured freshly and 4 d after the fabrication. The devices were stored under ambient condition (25 °C, 70%–80% RH) without any encapsulation. The performance of these devices shows less degradation than standard 3D $CH_3NH_3PbI_3$ solar cells (plotted in Figure S9, Supporting Information, for reference); the photocurrent density is reduced over the time while the photovoltage does not change significantly. The decrease in the performance could also be related to the degradation of perovskite layer by the additives in the hole transporting layer,[12] together with the decomposition of perovskite layer by oxygen and moisture. Thus, using an alternative hole transporting layer and with proper encapsulation of the device could increase its long-term stability. For a reference, *I* –*V* data of the standard 3D $CH_3NH_3PbI_3$ device deposited from single-step technique is displayed in Figure S10 (Supporting Information).

It has been shown that formamidinium lead iodide ($HC(NH_2)_2PbI_3$) possesses smaller bandgap as compared to $CH_3NH_3PbI_3$, allowing it to have a broader absorption window up to ≈840 nm.[29-31] However, the presence of the δ phase (yellow nonperovskite structure) in $HC(NH_2)_2PbI_3$ can reduce the performance and stability of the devices due to the phase transition noted at room temperature.[32] Several studies have shown

that mixing the CH_3NH_3I and formamidinium iodide ($HC(NH_2)_2I$) in 3D organolead halide perovskites is one of the most successful strategies in achieving high efficiency for photovoltaic devices.[32, 33] Similar strategy was implemented in our perovskite system where the as-spincoated $(IC_2H_4NH_3)_2PbI_4$ film was dipped into a mixed CH_3NH_3I and $HC(NH_2)_2I$ solution. **Figure 7**a shows the comparison of the optical absorption between the perovskite films fabricated from different dipping bath. According to Figure 7a, the absorption is wider for the mixed-dimensionality perovskite films formed from dipping in the mixed cations solution. This agrees with the observation in 3D organometal halide perovskite system. An overall power conversion efficiency over 9% was achieved and, to the best of our knowledge, this is the highest conversion efficiency for perovskite solar cells based on mixed-dimensionality perovskites.[16, 17]

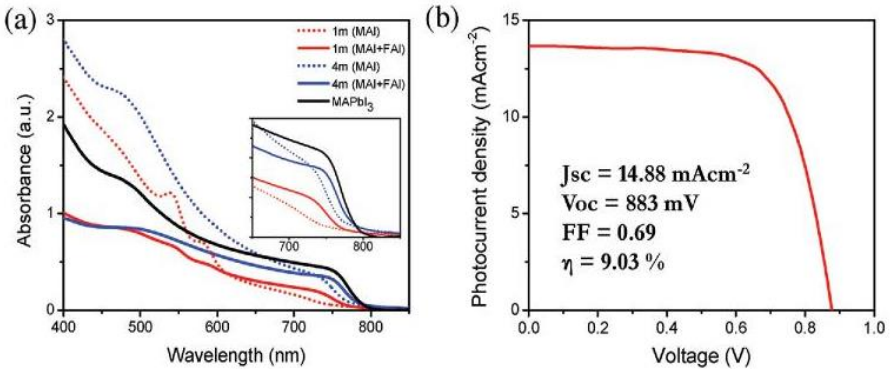

Figure 7. a) Enhanced optical absorption of mixed-dimensionality perovskites films by mixing CH_3NH_3I and $HC(NH_2)_2I$ (85:15) in dipping solution. b) Champion device with mix-dimensionality perovskites $(IC_2H_4NH_3)_2(CH_3NH_3)_{x\,(n-1)}(HC(NH_2)_2)_{y\,(n-1)}Pb_n\,I_{3n+1}$ fabricated by dipping in a mixed CH_3NH_3I:$HC(NH_2)_2I$ (85:15) solution in 4 min dipping time.

In conclusion, we have demonstrated a way to fabricate nanostructured mixed-dimensionality perovskites $(IC_2H_4NH_3)_2(CH_3NH_3)_{n-1}Pb_n\,I_{3n+1}$ and their application in photovoltaics. Our results strongly indicated the importance of the direction growth to the device performance in 2D perovskites solar cells. With preferentially oriented growth of 2D perovskites perpendicular to the substrate, the charge transport and extraction were drastically improved. By means of a mixed-organic cations approach, an overall conversion efficiency over 9% was achieved. Improvements in controlling surface coverage and effective blocking layer deployments would further enhance the device efficiency in reducing the interfacial recombination and hence improving the photovoltage of the devices. The nanostructuring approach thus offers a key advancement in deploying mixed-dimensional perovskite materials for high-efficiency solar cells. Additionally, it could be also effectively applied to alternative perovskites characterized by short charge diffusion lengths, where the photogenerated charges need to be efficiently transported and collected.

Experimental Section

Synthesis : 2-Iodoethylammonium iodide was synthesized by reacting 3 g of 2-bromoethylammonium bromide (Sigma-Aldrich, 99%) with 6 mL of hydriodic acid (Sigma-Aldrich, 99.99% 57 wt% in H_2O). 1 g of iodine (Sigma-Aldrich, ≥99.8%) was added into the solution. The solution was allowed to stir for 24 h and dried over rotary evaporator at 60 °C. The precipitate was recrystallized repeatedly using ethanol and diethyl ether until white color powder was obtained. Yield: 76%. Proton nuclear magnetic resonance ($_1$H NMR 400 MHz, DMSO-d_6): δ 7.83 (s, 3H), 3.25–3.16 (m, 4H).

Device Fabrication : The etched fluorine-doped tin oxide (FTO) substrates (Pilkington TEC 15) were cleaned by ultrasonication in decon-soap solution, deionized water, and ethanol, respectively. A compact layer of TiO_2 was coated onto the FTO substrate by spray pyrolysis process with titanium diisopropoxide bis(acetylacetonate) solution (Sigma-Aldrich, 75% in 2-propanol) diluted with ethanol (Sigma-Aldrich, ≥99.8%) in volume ratio of 1:9. After cooling to room temperature, the substrates were treated in a 50×10^{-3} m $TiCl_4$ solution (Wako Pure Chemical Industries, >99%) for 30 min at 70 °C. The substrates were washed with deionized water and dried with compressed air. The mesoporous TiO_2 film was formed by spin-coating DYESOL-30NRD paste (Dyesol, 30 nm TiO_2 nanoparticles), which was diluted with ethanol (Sigma-Aldrich, ≥99.8%) with a ratio of 1:3.5 w/w, and then sintered at 500 °C for 30 min. The films were then treated again with 50×10^{-3} m $TiCl_4$ solution at 70 °C for 30 min and heated at 500 °C again for 30 min. Prior to the perovskite deposition, the substrates were treated in UV-Ozone for 15 min. $(IC_2H_4NH_3)_2PbI_4$ film was deposited by spin-coating 1 m perovskite solution (dissolving 298.8 mg of the synthesized $IC_2H_4NH_3I$, with 230.5 mg of lead iodide, 99.99% from Sigma-Aldrich in 500 µL of anhydrous DMF, 99.8% from Sigma-Aldrich) onto the mesoporous film at 4000 rpm for 30 s. The substrate was then immersed into the CH_3NH_3I dipping solution (2 mL of 2-propanol was used to dissolve 24 mg of CH_3NH_3I, the clear solution is then diluted with 10 mL of toluene) for different dipping durations (1–5 min). After the substrate was removed from the dipping solution, it was directly immersed into the rinsing solution containing 2 mL of 2-propanol and 10 mL of toluene to remove unreacted CH_3NH_3I residue. For the standard 3D devices, $CH_3NH_3PbI_3$ perovskite film was obtained by spin-coating 1 m of $CH_3NH_3PbI_3$ DMF solution on the mesoporous TiO_2 layer at 2000 rpm for 30 s. The film was then annealed at 100 °C for 10 min. 2,2′,7,7′-Tetrakis(*N* ,*N* ′-di-*p* -methoxyphenylamine)-9,9′-spirobifluorene (spiro-OMeTAD, Merck livilux SHT-263) was prepared in anhydrous chlorobenzene (Sigma-Aldrich, 99.8%) with a concentration of 100 mg mL^{-1}. 15.92 µL of *tert* -butylpyridine (96% from Sigma-Aldrich) and 9.68 µL of lithium bis(trifluoromethylsulfonyl)imide (99.95% from Sigma-Aldrich, 520 mg mL^{-1} in acetonitrile) were added directly to the 300 µL of spiro-OMeTAD solution. 3.6 mg of tris(2-(1*H* -pyrazol-1-yl)pyridine)cobalt(III) tris(hexafluorophosphate) *Co* -dopant (FK102, synthesized according to literature$_1$) was predissolved into 13 µL of anhydrous acetonitrile (Sigma-Aldrich, 99.8%) and added into the hole-transport material solution. The as-prepared spiro-OMeTAD solution was spin-coated onto the perovskite film at 4000 rpm for 30 s. A 100 nm Au cathode layer was deposited by thermal evaporation with a 0.2 cm^2 metallic mask. All the fabrication processes and device characterizations were conducted outside the glove-box.

Characterization : Photovoltaic measurements utilized an AM 1.5G solar simulator equipped with a 450 W xenon lamp (model 81172, Oriel). Its power output was adjusted to match AM 1.5G sunlight (100 mW cm^{-2}) by using a reference Si photodiode. *I* –*V* curves were obtained by applying an external bias (100 mV s^{-1} for both forward and backward scans) to the cell and measuring the generated photocurrent with a Keithley model 2612A digital source meter. A total of 31 devices were measured by masking the active area with a black tape mask. The absorption spectra were obtained using a UV–vis spectrometer (SHIMADZU UV-3600 UV–vis-NIR Spectrophotometer) with an integrating sphere (ISR-3100). The morphology features and cross-sectional images of devices were observed using a FESEM (JOEL JSM

6700F). XRD patterns of perovskite films were collected using a Bruker D8 Advance diffractometer fitted with a Cu Kα source operated at 40 kV and 40 mA, a 1° divergence slit, 0.3 mm receiving slit, a secondary graphite monochromator, and a Lynxeye silicon strip detector. GIWAXS measurements were conducted in vacuum using a Ganesha 300XL SAXS-WAXS system with an incident angle of 0.4° and a sample-detector distance of ≈110 mm. The exact value of the sample-detector distance was calibrated for each measurement individually according to the Bragg peaks observed in XRD. For data evaluation, the software GIXSGUI was used with appropriate data corrections offered by the software. Inaccessible data due to detector gaps were amended by using the symmetry of the scattering pattern, while the data in the inaccessible wedge around $q_r = 0$ Å^{-1} arising from experimental geometry was recovered by assuming a Gaussian peak shape. The data shown are summed up from individual shorter measurements giving a total integration time of about 14 h.

Acknowledgements

T.M.K. and V.S. contributed equally to this work. The authors would like to acknowledge the funding from Singapore NRF through the Competitive Research Program: NRF-CRP4-2008-03 and NRF-CRP14-2014-03 as well as from NTU-A*STAR Silicon Technologies Centre of Excellence under the program grant no. 112 3510 0003. J.S., L.O., and P.M.-B. thank for funding from the Excellence Cluster "Nanosystems Initiative Munich" (NIM) and the Bavarian Collaborative Research Project "Solar Technologies Go Hybrid" (SolTech). Treatment of GIWAXS data was conducted using the software GIXSGUI provided free of charge by Advanced Photon Source, Argonne National Laboratory, USA.

References

[1] J. H. Im, C. R. Lee, J. W. Lee, S. W. Park, N. G. Park, *Nanosca!e* **2011**, *3*, 4088.
[2] H. S. Kim, C. R. Lee, J. H. Im, K. B. Lee, T. Moehl, A. Marchioro, S. J. Moon, R. Humphry-Baker, J. H. Yum, J. E. Moser, M. Grätzel, N. G. Park, *Sci. Rep.* **2012**, *2*, 591.
[3] Y. Cao, J. Zhang, Y. Bai, R. Li, S. M. Zakeeruddin, M. Graetzel, P. Wang,*J. Phys. Chem. C* **2008**, *112*, 13775.
[4] W. S. Yang, J. H. Noh, N.J. Jeon, Y. C. Kim, S. Ryu, J. Seo, S. I. Seok, *Science* **2015**, *348*, 1234.
[5] P. P. Boix, S. Agarwala, T. M. Koh, N. Mathews, S. G. Mhaisalkar,*J. Phys. Chem. Lett.* **2015**, *6*, 898.
[6] P. Docampo, S. Guldin, T. Leijtens, N. K. Noel, U. Steiner, H. J. Snaith, *Adv. Mater.* **2014**, *26*, 4013.
[7] G. Xing, N. Mathews, S. S. Lim, N. Yantara, X. Liu, D. Sabba, M. Grätzel, S. Mhaisalkar, T. C. Sum, *Nat. Mater.* **2014**, *13*, 476.
[8] S. D. Stranks, G. E. Eperon, G. Grancini, C. Menelaou, M. J. P. Alcocer, T. Leijtens, L. M. Herz, A. Petrozza, H. J. Snaith, *Science* **2013**, *342*, 341.
[9] G. C. Xing, N. Mathews, S. Y. Sun, S. S. Lim, Y. M. Lam, M. Grätzel, S. Mhaisalkar, T. C. Sum, *Science* **2013**, *342*, 344.
[10] G. Niu, W. Li, F. Meng, L. Wang, H. Dong, Y. Qiu,*J. Mater. Chem. A* **2014**, *2*, 705.
[11] J. M. Frost, K. T. Butler, F. Brivio, C. H. Hendon, M. van Schilf-gaarde, A. Walsh, *Nano Lett.* **2014**, *14*, 2584.
[12] W. Li, H. Dong, L. Wang, N. Li, X. Guo, J. Li, Y. Qiu,*J. Mater. Chem. A***2014**, *2*,13587.
[13] S. Ito, S. Tanaka, K. Manabe, H. Nishino,*J. Phys. Chem. C* **2014**, *118*, 16995.
[14] T. Leijtens, G. E. Eperon, S. Pathak, A. Abate, M. M. Lee, H. J. Snaith, *Nat. Commun.* **2013**, *4*, 2885.

[15] J. H. Noh, S. H. Im, J. H. Heo, T. N. Mandal, S. I. Seok, *Nano Lett.* **2013**, *13*, 1764.
[16] I. C. Smith, E. T. Hoke, D. Solis-Ibarra, M. D. McGehee, H. I. Karunadasa, *Angew. Chem. Int. Ed.* **2014**, *53*, 11232.
[17] D. H. Cao, C. C. Stoumpos, O. K. Farha, J. T. Hupp, M. G. Kanatzidis,*J. Am. Chem. Soc.* **2015**, *137*, 7843.
[18] T. Ishihara,*J. Lumin.* **1994**, *60*, 269.
[19] D. B. Mitzi, *Chem. Mater.* **1996**, *8*, 791.
[20] D. B. Mitzi,*J. Mater. Chem.* **2004**, *14*, 2355.
[21] W. Shockley, H. J. Queisser,*J. App!. Phys.* **1961**, *32*, 510.
[22] X. Wu, M. T. Trinh, X. Y. Zhu,*J. Phys. Chem. C***2015**, *119*, 14714.
[23] M. I. Saidaminov, A. L. Abdelhady, B. Murali, E. Alarousu, V. M. Burlakov, W. Peng, I. Dursun, L. Wang, Y. He, G. Maculan, A. Goriely, T. Wu, O. F. Mohammed, O. M. Bakr, *Nat. Commun.* **2015**, *6*, 7586.
[24] Y. Han, S. Meyer, Y. Dkhissi, K. Weber, J. M. Pringle, U. Bach, L. Spiccia, Y.-B. Cheng,*J. Mater. Chem. A* **2015**, *3*, 8139.
[25] V. L. P. Guerra, D. Altamura, V. Trifiletti, S. Colella, A. Listorti, R. Giannuzzi, G. Pellegrino, G. G. Condorelli, C. Giannini, G. Gigli, A. Rizzo,*J. Mater. Chem. A* **2015**,*3*, 20811.
[26] Z. Cheng, J. Lin, *Cryst. Eng. Commun.* **2010**, *12*, 2646.
[27] . Dharani, H. A. Dewi, R. R. Prabhakar, T. Baikie, C. Shi, Y. Du, N. Mathews, P. P. Boix, S. G. Mhaisalkar, *Nanoscale* **2014**, *6*, 13854.
[28] N. Yantara, D. Sabba, F. Yanan, J. M. Kadro, T. Moehl, P. P. Boix, S. Mhaisalkar, M. Graetzel, C. Graetzel, *Chem. Commun.* **2015**, *51*, 4603.
[29] T. M. Koh, K. Fu, Y. Fang, S. Chen, T. C. Sum, N. Mathews, S. G. Mhaisalkar, P. P. Boix, T. Baikie,*J. Phys. Chem. C* **2014**, *118*, 16458.
[30] G. E. Eperon, S. D. Stranks, C. Menelaou, M. B. Johnston, L. M. Herz, H. J. Snaith, *Energy Environ. Sci.* **2014**, *7*, 982.
[31] J.-W. Lee, D.-J. Seol, A.-N. Cho, N.-G. Park, *Adv. Mater.* **2014**, *26*, 4991.
[32] N.J. Jeon, J. H. Noh, W. S. Yang, Y. C. Kim, S. Ryu, J. Seo, S. I. Seok, *Nature* **2015**, *517*, 476.
N. Pellet, P. Gao, G. Gregori, T.-Y. Yang, M. K. Nazeeruddin, J. Maier, M. Grätzel, *Angew. Chem. Int. Ed.* **2014**, *53*, 3151.